

## Research Article

# Pullout Behavior of GFRP Anti-Floating Anchor Based on the FBG Sensor Technology

Ming-yi Zhang,<sup>1</sup> Zheng Kuang ,<sup>1</sup> Xiao-yu Bai ,<sup>1</sup> and Xiao-yu Chen<sup>2</sup>

<sup>1</sup>College of Civil Engineering, Qingdao University of Technology, Qingdao, Shandong 266033, China

<sup>2</sup>Faculty of Construction and Environment, The Hong Kong Polytechnic University, Hung Hom, Hong Kong

Correspondence should be addressed to Zheng Kuang; kz9403@163.com

Received 28 June 2018; Revised 29 September 2018; Accepted 12 December 2018; Published 27 December 2018

Academic Editor: Nicolas J. Leconte

Copyright © 2018 Ming-yi Zhang et al. This is an open access article distributed under the Creative Commons Attribution License, which permits unrestricted use, distribution, and reproduction in any medium, provided the original work is properly cited.

Building anti-floating anchors have been increasingly used in recent years, but conventional steel anchors under service conditions are easily subjected to chemical erosion. Glass fiber reinforcement polymer (GFRP) is a promising solution to this problem. In this study, field pullout tests were conducted on three full instrumented GFRP anti-floating anchors in weathered granite. Specifically, the GFRP anchors during pultrusion were innovatively embedded with bare fiber Bragg grating (FBG) sensors to monitor the axial force distribution along depth. It was found that the embedded FBG could reliably monitor the axial force distribution of GFRP anchors. The ultimate pullout force of a GFRP anchor with diameter of 28 mm and anchorage length of 5 m was up to 400 kN. The GFRP anchor yielded at 0.8 m underground. Force distribution and field photos at failure indicated shear failure occurred at the anchor/bolt interface at the end of the tests. The feasibility of the GFRP anti-floating anchor was also verified in civil engineering. Finally, an elastic mechanical model and Mindlin's displacement solution are used to get distribution functions of axial force and shear stress along the depth, and the results accord with the test results.

## 1. Introduction

Building floating issues due to the increasingly larger and deeper underground basement at high water level have attracted wide attention recently. The anti-floating anchor, a kind of anti-floating method through connecting the anchor and soil, is widely used to solve these issues owing to its lower cost, shorter construction period, strong stratum adaptability, and less point force than traditional methods (kentledge, anti-floating pile, and drainage) [1–3]. However, due to the corrosive ions in groundwater, the ordinary steel anchor under aggressive environment inevitably suffers from chemical erosion, which seriously weakens the long-term structure strength.

Moreover, the stray current produced from the direct current power system subjects metal anchors to electrochemical erosion, especially in urban rail projects [4]. In order to solve the problems mentioned above, nonmetallic anchors appear [5].

Nowadays, glass fiber reinforcement plastic (GFRP), fabricated by extruding molten glass through an orifice, is one

of the most popular alternatives of all fiber reinforcement plastics owing to its lower cost, higher tensile strength, and excellent insulation [6]. In-depth investigations of GFRP properties including pull-out performance and mechanism compared to ordinary steel anchors suggest (a) GFRP bars could alternate ordinary steel bars in most projects based on model tests and (b) the GFRP bar, owing to lower elasticity modulus, has a larger slippage at failure than steel bars [7]. What is more, a series of experiments have been conducted and revealed that higher concrete strength is beneficial for improving the pullout capacity and bond durability of GFRP anchor [8, 9]. However, GFRP bars and furthermore GFRP bars as anti-floating anchors are still unfamiliar to practicing Chinese engineers.

The force transfer mechanism and failure mode of GFRP anti-floating anchors should be comprehensively studied to encourage their use in buildings. For this purpose, the first investigation should be the measurement method of axial force along depth. Conventionally, the axial force along depth is monitored by strain gage or fiber Bragg grating (FBG) sensors directly attached on the anti-floating anchor.

TABLE 1: Mechanical parameters of test field.

Uniaxial compressive strength	Unit weight	Poisson ratio	Elastic modulus
32 MPa	24.5 kN/m <sup>3</sup>	0.33	35 MPa

However, these sensors may fall off during anchor installation and pullout tests. Another option is to embed a sensor in the anchor by initially cutting the anchor body, but the cutting-produced defects seriously damage the integrity of fiber reinforcing anchors, reducing the pullout strength of the anchor [10].

In this study, field pullout tests were conducted on three full-instrumented GFRP anti-floating anchors installed into rock base, and the naked FBG was innovatively embedded into the anchors during pultrusion to monitor the axial force. This study aimed to (a) verify the applicability of the GFRP anti-floating anchors in rock base, (b) evaluate the feasibility of FBG installation on these anchors, (c) investigate the head-displacement response of these anchors during pullout tests, and (d) study the load transfer mechanism and failure mode based on field tests.

## 2. Pullout Test Program

**2.1. Description of Field Geology.** The test field, with soft rock, contains moderately weathered granite and other mechanical parameters are shown in Table 1.

**2.2. Installation of the FBG Sensor.** Wavelength  $\gamma_B$  of FBG, which varies with the temperature and structure strain at the granted region, could be directly measured during whole tests [11]. Due to the less time during whole tests and stable underground temperature, the temperature change during whole tests is small enough to be ignored, and the strain along the anchor is simplified as

$$\Delta\varepsilon = \frac{\Delta\gamma_B}{K_e} \quad (1)$$

where  $\Delta\varepsilon$  is the strain along the anchor and  $K_e$  is strain sensitivity coefficient of FBG.

The naked FBG was innovatively embedded into each GFRP anchor: we firstly embed the FBG sensor in the center of the glass fiber bundle along the longitudinal direction of the rod body and place into the mold and then pour the anchor base material (synthetic resin), through the procedures of pultrusion, thread winding, and solidification; GFRP anchor rod body is manufactured. Naked optional fiber of SMF28-C, diameter of 900  $\mu\text{m}$ , was selected here due to its low volume, high temperature resistance, and ease in installation. Bragg gratings (details in Table 2) were distributed along the naked optional fiber as illustrated in Figure 1.

To prevent FBG sensors from damage during the tests, we put the sensors into a capillary tube and encapsulated them by filling with hot epoxy resins by needles. The tip of the FBG was weld with 3-interdiameter armored cable, covered by

TABLE 2: Parameters of Bragg gratings.

Type	Length	Reflection rate	Width	SLSR
Bragg gratings	10 mm	80%	0.3 nm	15 dB

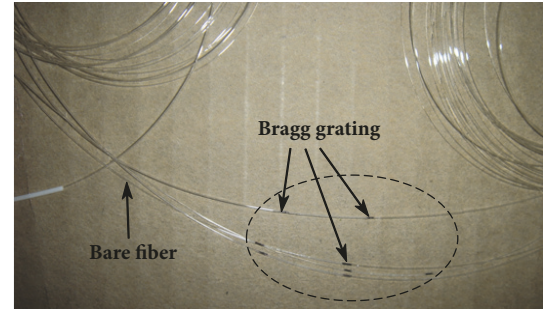


FIGURE 1: Photo of FBG sensors.

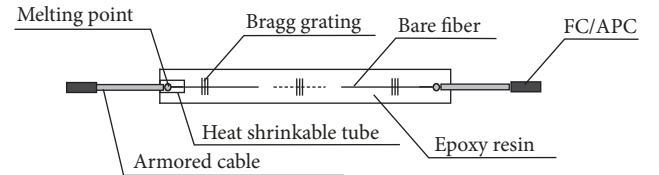


FIGURE 2: Schematic view of encapsulated FBG sensors.

polymer to blend and protect the connection, and finally the connection was put with heat shrinkable tubing (Figure 2).

The encapsulated FBG sensors were embedded in the GFRP anchors during the pultrusion. The survival rates of FBG sensors before full-scale tests were evaluated by both laboratory and field tests. Results show all FBG sensors worked well even at failure of anchors. Hence, the innovative FBG installation technique not only maintains the integrity of GFRP anchors, but also provides more high-resolution results.

**2.3. Description of GFRP Anchors.** All GFRP anchors (YF-H50-28) embedded with FBG sensors were manufactured by the pultrusion process in a Chinese company, and the properties were 75% glass fiber + 25% resin (unsaturated polyester resin), with section area = 590 mm<sup>2</sup>, density = 2.1 g/cm<sup>3</sup>, and weight = 1195 g/m (Figure 3). Accessory ingredients such as curing agent and accelerant are also applied during the anchor manufacture process. Each anchor at the hole center was supported by a centralizer (Figure 3). Three GFRP anti-floating anchors, named GFRP-01, 02, and 03 with a nominal diameter of 28 mm, total length of 6.5 m, and anchorage length of 5 m, were used in the tests. Mechanical parameters of GFRP anchors (Table 3) indicate that the tensile strength is 1.5-2.4 times and the modulus of elasticity is 20% that of ordinary steel bars. Figure 4 shows the arrangement of the FGB sensors along depth.

**2.4. Pullout Test.** Holes were drilled vertically by an in-the-hole-drill, in diameter of 110 mm and length 0.5 m larger than the anchor length. A GFRP anchor then was vertically

TABLE 3: Mechanical parameters of GFRP bar.

Type	Tensile strength	Shear strength	Ultimate load	Elastic modulus
GFRP bar	702 MPa	150 MPa	432 KN	51 MPa

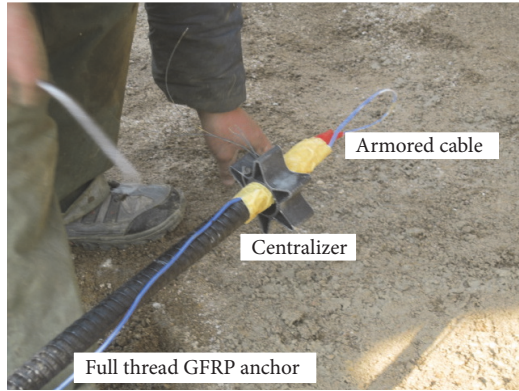


FIGURE 3: Photo of GFRP anchor.

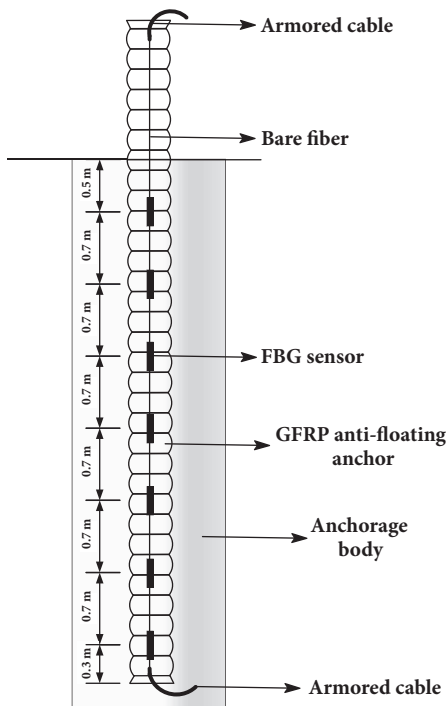


FIGURE 4: Anchor bolt after installing FBG sensors.

placed into the hole by workers and fixed at the hole center by centralizers. Finally, M32.5 cement mortar was poured into the hole.

Due to the low shear resistance of GFRP bars, stress concentration at the anchorage would damage the GFRP anchor. To protect and hold the GFRP anchor, we innovatively applied one steel tube with diameter, length, and wall thickness of 1.2 mm, 50 mm, and 5 mm, respectively, before mounting a clip anchorage on the anchor. The tube was filled with a mixture of epoxy resin and curing agent to form a strong

bond on tube and GFRP anchor. In order to guarantee that the mixture fills the tube, we firstly smear the mixture on the anchor surface and then continuously rotate the tube so that the mixture fills the inner wall of the tube, until the inner wall is filled. The test devices are presented in Figure 5.

In accordance with *Chinese Technical Code*, field pullout tests were conducted at a slow applied rate of 0.2 kN/s, without loading-unloading loops. The first stage load was 50 kN, and the subsequent stage loads were kept at magnitudes 100, 150, and 200 kN to the failure state. The displacement of anchor head is read immediately after each stage.

### 3. Results and Discussion

**3.1. Head Displacement Response.** Head displacement response of each GFRP anchor during whole tests is presented in Figure 6. The head displacement is elevated linearly, without significant fluctuation, along with the increasing pullout force, which is different from the ordinary steel anchor undergoing a sudden increase at failure [12]. This difference could be attributed to the lower elastic modulus of GFRP. In addition, the GFRP anchor outperformed the steel anchor in terms of elongation at failure. The ultimate pullout force of the 28-mm-diameter GFRP anchor is defined as 400 kN in accordance with *Chinese Technical Code* [13], which is higher than that (345 kN) of the steel anchor under the same condition (Bai et al. [14]). Thus, the GFRP anti-floating anchor not only resists chemical erosion, but also provides higher pullout capacity in anti-floating structures.

**3.2. Distribution of Axial Force.** Figure 7 shows the distribution of axial force along depth during whole tests, which was calculated as follows, assuming the same transformation between FBG sensors and anchor:

$$N_i = E_G A_G \cdot \Delta \varepsilon_i = E_G A_G \cdot \frac{\gamma_{Bi}}{K_e} \quad (2)$$

where  $\Delta \varepsilon_i$  is the strain at FBG sensor  $i$ ;  $N_i$  is the axial force at FBG sensor  $i$ ; and  $E_G$  and  $A_G$  are Young's modulus and cross-sectional area of the GFRP anchor, respectively.

Axial force along the GFRP anchor significantly decreased at depth of 0~3 m, while the deeper part supported relatively less pullout force, which indicates the nonuniform mobilization of axial force along the GFRP anchor.

The distribution of axial force along depth also suggests the presence of a critical load transfer depth for the GFRP anchor. Specifically, little force transfer to the anchor below 3~3.5 m was found in GFRP-01, 02, and 03, which means prolonging the anchor length, when it is up to the critical depth, does not obviously enhance the pullout force. The conclusion is consistent with the research results by Bai et al. [14]. However, adhesion between rock and anchorage bolt cannot be guaranteed if an over-short anchor length is employed.

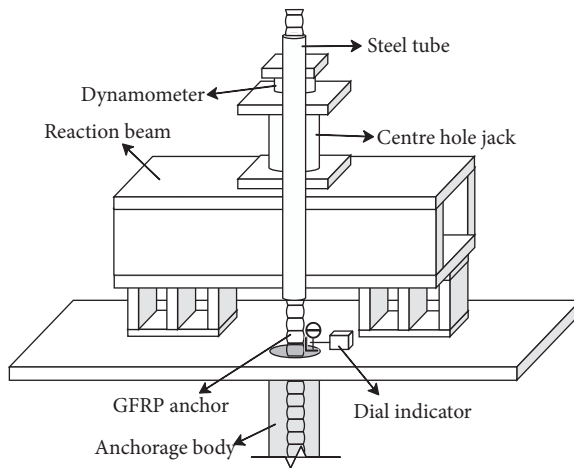


FIGURE 5: Photo of pull-out test devices.

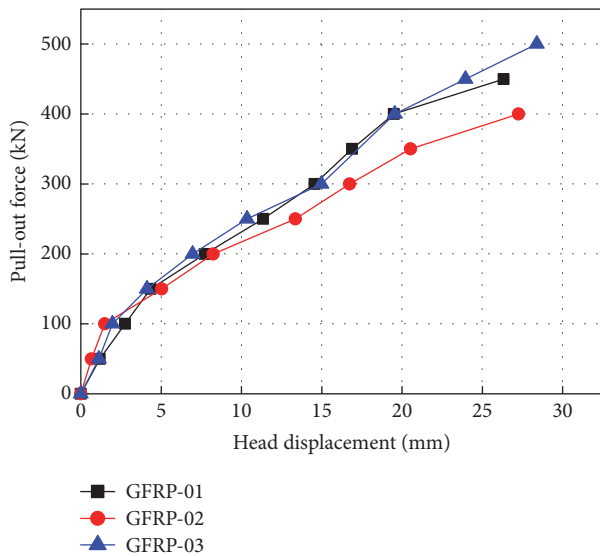


FIGURE 6: Head displacement response.

Nevertheless, further research is needed to determine the critical depth under different conditions.

The maximum measured axial force of GFRP anchors at failure is smaller than the ultimate tensile strength (500 kN vs 702 kN), which can be explained by the local failure along the GFRP anchor.

**3.3. Distribution of Shear Stress.** Figure 8 presents the shear stress distribution along depth during whole tests, which can be calculated as follows by assuming the uniform distribution of load between two contiguous FBG sensors:

$$\tau_i = \frac{(N_i - N_{i-1})}{\pi d \Delta L} \quad (3)$$

where  $\tau_i$  is the shear stress along depth at point  $i$ ;  $d$  is the diameter of the GFRP anchor; and  $\Delta L$  is the distance between two contiguous FBG sensors.

The peak shear stress along depth was elevated and its influence area was enlarged with the increasing applied pullout force. The maximum shear stress reached 3~4 MPa at failure. Compared to the steel anchor with peak shear stress appearing at ground surface, the peak of GFRP anchors occurred at 0.8 m underground, which is consistent with a previous study [15]. This difference can be explained by the low stiffness of the GFRP anchor: GFRP anti-floating anchors produce greater elastic deformation when bearing pullout loads and cause obvious deformation of the anchor section near the hole so that the anchor bolt and grouting body show the shear slip. Hence, the anchor separates with surrounding concrete that means a lower shear stress at their interface. The shear slip between the anchor bolt and grouting body will reduce with the increase of the anchor depth, so the shear stress would also increase; when the shear slip reduces to 0, the shear stress increases to the maximum. Figure 8 also indicates that additional reinforcement at 0.8 m underground is required if a GFRP anti-floating anchor is used in projects.

**3.4. Failure Mode.** When the pullout force is up to 60%-70% of the ultimate loading, the GFRP anchor produces slight crack noise, and its head displacement rises constantly with 8-10 cm crack around anchorage body (Figure 9). Relative slippage between the anchor and anchorage bolt occurred at failure (all test anchors) (Figure 10(a)); surface fiber got pilled off and white-spot crack appeared on surface (only GFRP-02 anchor) (Figure 10(b)); a part of the fiber plate was detached (only GFRP-03 anchor) (Figure 10(c)). Installing additional ribs on the anchor surface could solve the problem of fiber plate detachment [16].

From the pictures of GFRP anchors at failure, it is figured out that the damage of GFRP anchors occurred at the anchorage part instead of the free part that supported the

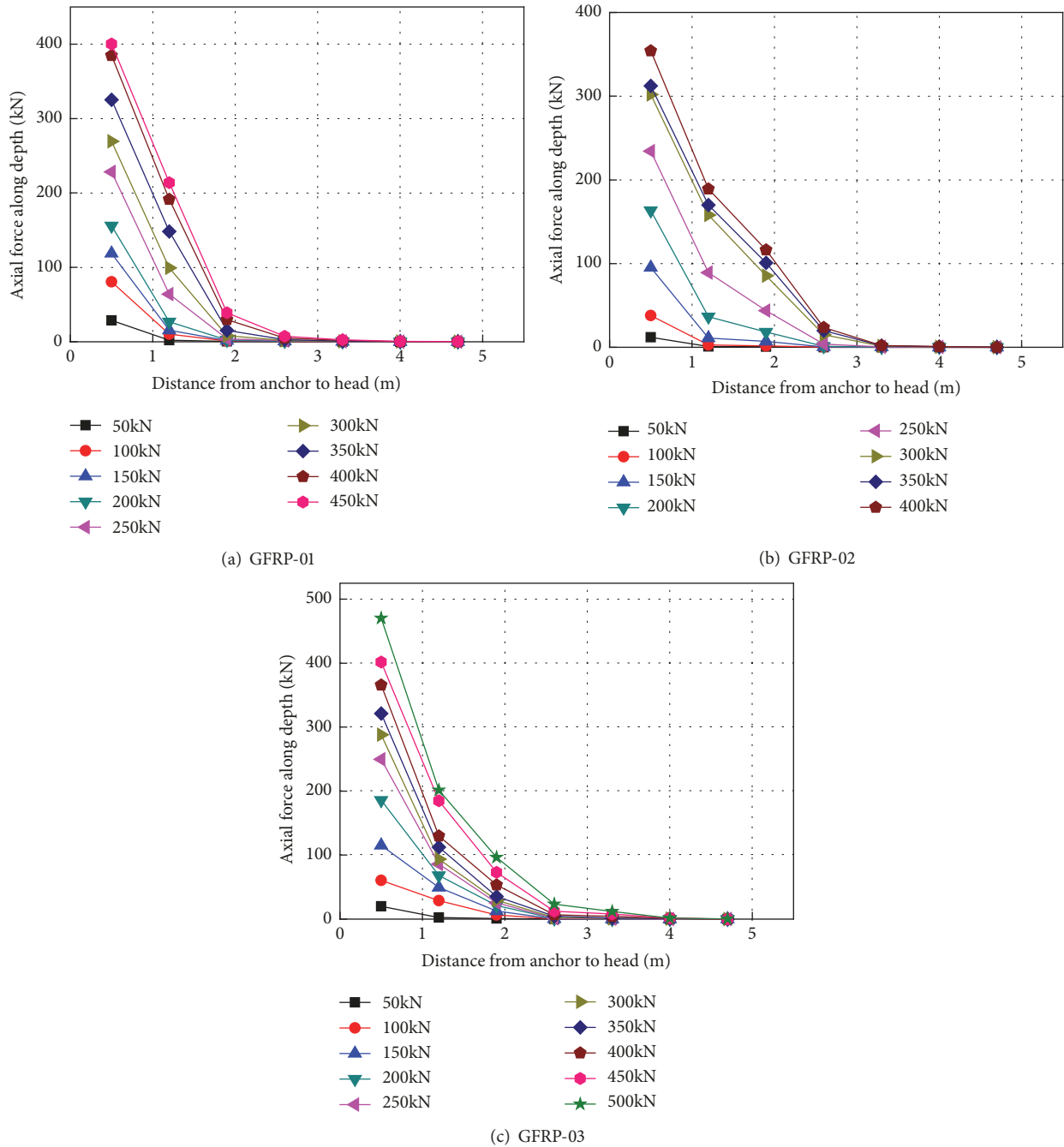


FIGURE 7: Distribution of axial force along depth.

largest pull force. In addition, the shear stress was maximized at 0.8 m underground, which is consistent with the failure location. These results indicate that the failure mode is shear failure rather than pull-out failure.

#### 4. Theoretical Analysis

We introduced the mathematical function model studied by You [17] to predict the distribution rule of anchor's axial force and shear stress, which is beneficial for avoiding the disadvantages of the above-mentioned test, such as high cost and time waste. Assuming that the anchor is an elastomer and

the properties are the same for both rock mass and anchorage body, we have an analytical model for a fully grouted anchor which is described in detail in Figure 11. The pullout force, shear stress, the length of the unit, axial force, and shear stress in a certain depth are denoted by  $P$ ,  $\tau$ ,  $dx$ ,  $P(x)$ , and  $\tau(x)$ , respectively.

Taking into account the static equilibrium condition, we obtain the following relations:

$$dp(x) = -2\pi r\tau(x) dx \tag{4}$$

where  $r$  is the radius of the anchor.

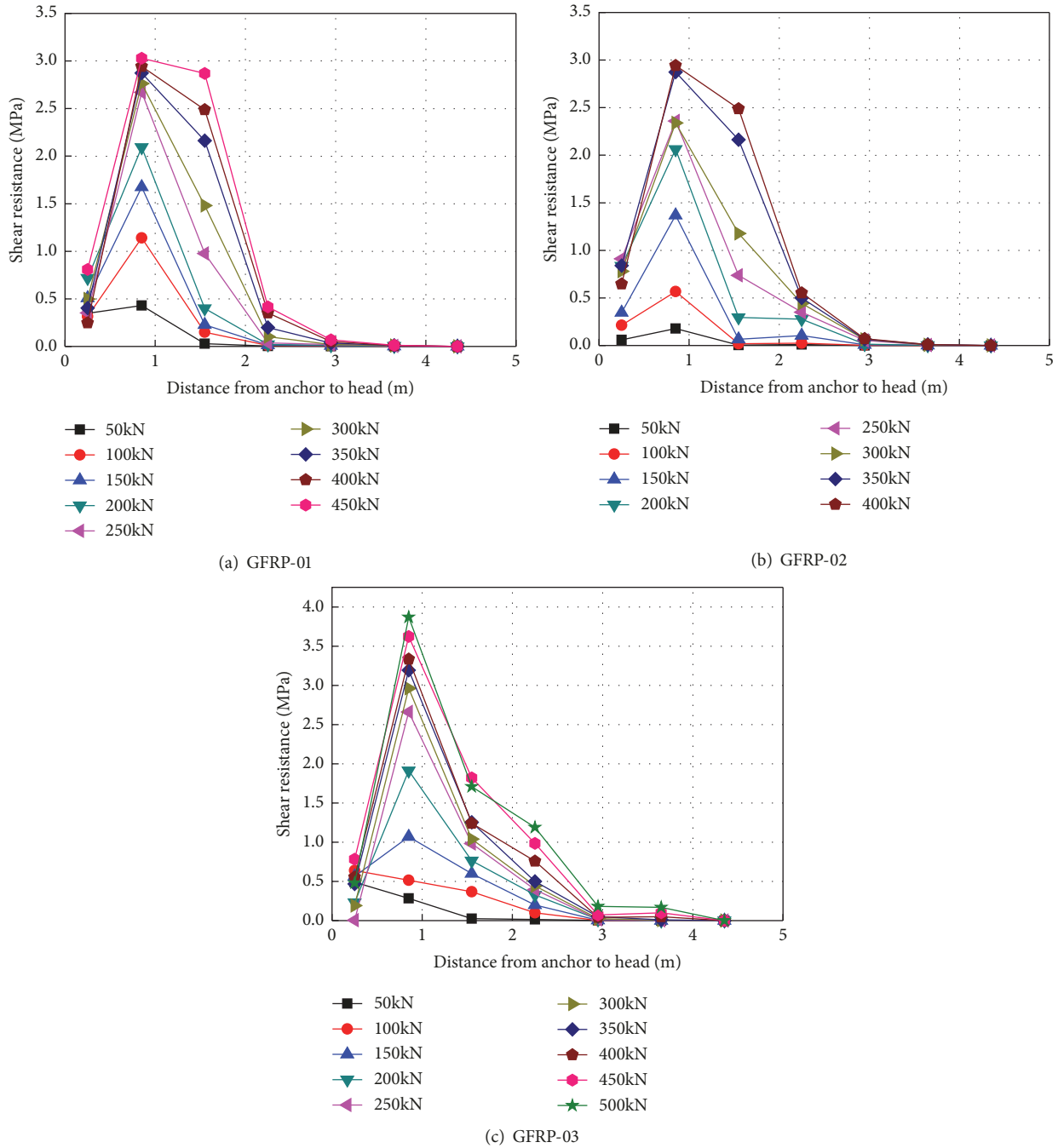


FIGURE 8: Distribution of shear stress along depth.

Then, integrating the above formula, we obtain the relation for  $P(x)$  and  $\tau(x)$ :

$$P(x) = -2\pi r \int_x^{L_a} \tau(x) dx \quad (5)$$

where  $L_a$  is the anchorage length of the anchor.

As depicted in (5),  $\tau(x)$  is the key issue to reach the aim of this investigation.

We will now introduce Mindlin's displacement solution to get the equation for  $\tau(x)$ . The assumption of the solution is that the rock mass is semi-infinite space, the origin of

coordinates is located at the hole, and the anchor is along the  $x$ -axis. As shown in Figure 12, when a concentrated force, with the depth of  $c$ , is applied at the point A, the vertical displacement of the point B ( $x, y, z$ ) can be expressed as

$$s = \frac{Q(1+\mu)}{8\pi E(1-\mu)} \left[ \frac{3-4\mu}{R_1} + \frac{8(1-\mu)^2 - (3-4\mu)}{R_2} \right] + \frac{(x-c)^2}{R_1^3} + \frac{(3-4\mu)(x+c)^2 - 2cx}{R_2^3}$$



FIGURE 9: Cracks on anchorage body at failure.



(a) Relative slippage between the anchor and anchorage bolt



(b) Surface white-spot crack



(c) Fiber plate detachment

FIGURE 10: GFRP anchors at failure.

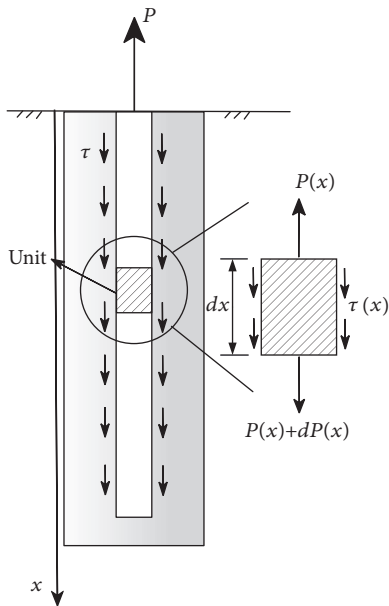


FIGURE 11: Mechanical model for a fully grouted anchor.

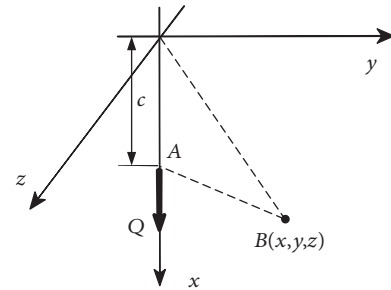


FIGURE 12: Schematic of Mindlin's displacement solution.

where  $E$ ,  $\mu$  are elastic modulus and Poisson ratio of the rock mass, respectively;

$$R_1 = \sqrt{y^2 + z^2 + (x - c)^2}; \tag{7}$$

$$R_2 = \sqrt{y^2 + z^2 + (x + c)^2}.$$

At the origin of coordinates ( $x = y = z = 0$ ), the expression of (6) becomes

$$\left[ + \frac{6cx(x+c)^2}{R_2^5} \right] \tag{6}$$

$$s_o = \frac{Q(1+\mu)(3-2\mu)}{2\pi cE} \tag{8}$$

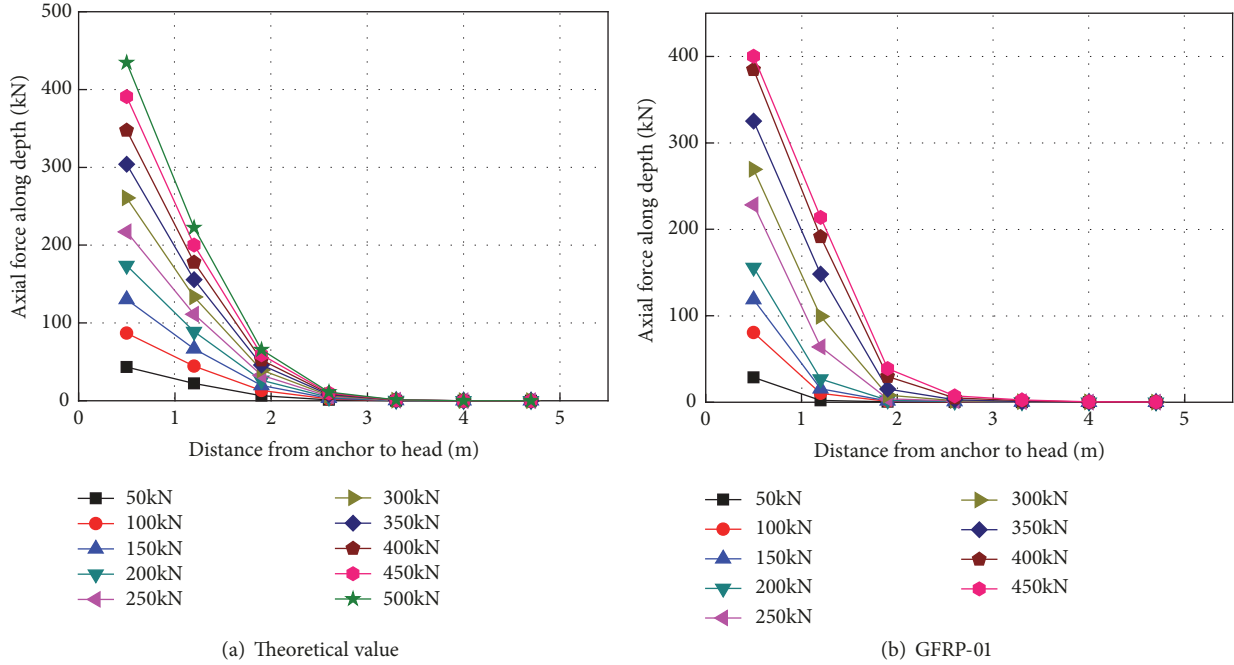


FIGURE 13: Distribution of axial force along the depth.

For the rock mass,  $Q$  signifies the shear stress that the pullout force exerts on the rock mass at the point  $A$ , which is expressed as

$$Q = 2\pi r \tau \cdot dx \quad (9)$$

Additionally, for the anchor,  $Q$  denotes the pullout force transferred to the point  $A$ . So the elastic elongation of the anchor can be calculated as

$$\frac{Q - 2\pi r \int \tau dx}{E_a \cdot \pi r^2} \quad (10)$$

where  $E_a$  is the elastic modulus of the anchor.

We then assume that the anchor is a semi-infinite bolt and deforms with rock mass compatibility. The elongation of the anchor at the hole is the same as the displacement of the rock mass; the equation can be expressed as

$$\int_0^\infty \frac{Q - 2\pi r \int \tau(x) dx}{E_a \cdot \pi r^2} dx = \int_0^\infty \frac{2\pi r \tau(x) \cdot (1 + \mu)(3 - 2\mu)}{2\pi x E} dx \quad (11)$$

After simplifying (11), we obtain a differential equation:

$$\tau''(x) + \left(kx - \frac{2}{x}\right) \tau'(x) + \frac{2}{x^2} \tau(x) = 0 \quad (12)$$

where  $k = 2E/(1 + \mu)(3 - 2\mu)E_a r^2$ .

Transforming (12) to Weber equation [18], then substitute boundary condition,  $x \rightarrow \infty, \tau = 0$ , into it;  $\tau(x)$  can be determined as

$$\tau(x) = \frac{P}{\pi r} \left(\frac{\lambda}{2} x\right) \cdot e^{-(\lambda/2)x^2} \quad (13)$$

where  $P$  is the pullout force;

$$\lambda = \frac{E}{E_a (1 + \mu)(3 - 2\mu) r^2}. \quad (14)$$

Substituting (13) into (5), we obtain the distribution of axial force:

$$P(x) = P \cdot e^{-(\lambda/2)x^2} \quad (15)$$

To verify the correctness of (13) and (15) above, we substitute the parameters of this test in them, and the results are shown in Figures 13(a) and 14(a).

As shown in Figures 13 and 14, compared with the test result, the theoretical results are accurate, which prove the correctness of the above-mentioned theoretical analysis for GFRP anti-floating anchor.

## 5. Conclusion

This paper presents and primarily analyzes the field pullout tests on three GFRP anti-floating anchors in weathered granite under service condition. The feasibility of embedded FBG technique was also verified.

(a) The innovative embedded FBG technique is able to monitor axial force accurately during whole tests, with survival rate of 100%. This technique keeps the integrity of GFRP anchors and provides reference for the monitoring of anisotropic materials.

(b) GFRP anti-floating anchors have the ultimate pullout force (400 kN) up to 2 times that of steel anchors and thus could replace conventional steel anchors in projects.

(c) Different from steel anchors, the head displacement of GFRP anchors increases linearly with the applied load and

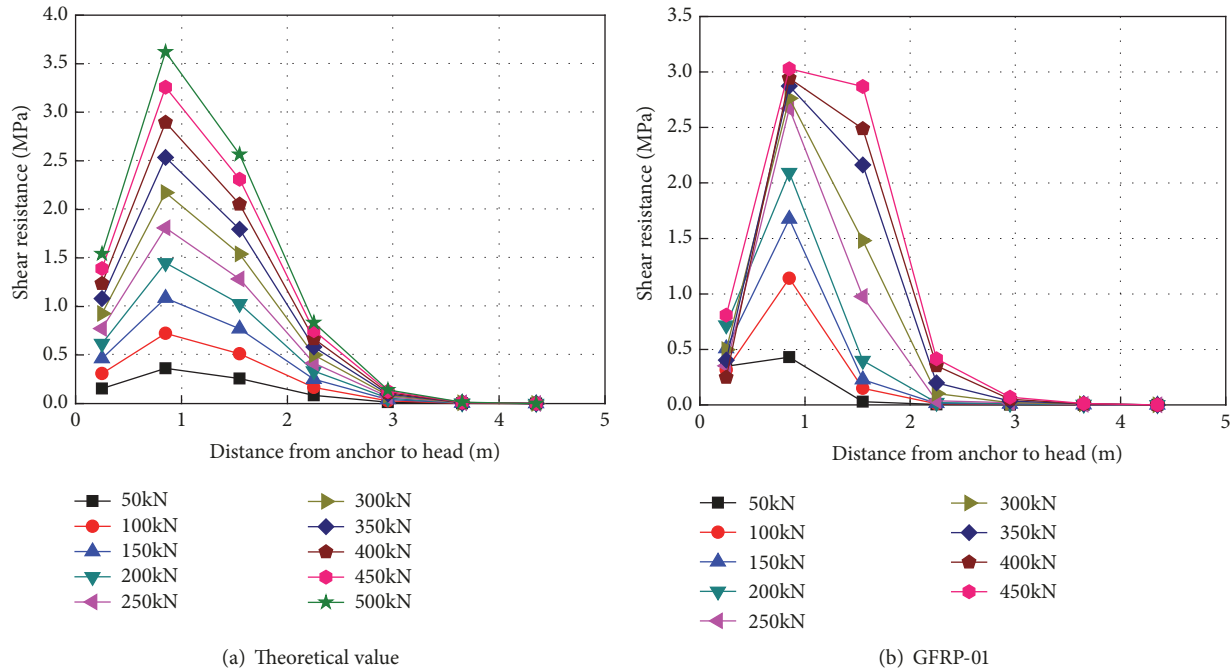


FIGURE 14: Distribution of shear stress along the depth.

has larger elongation before failure, which could be explained by their less elastic-modulus.

(d) No pullout force was transferred to 3.5 m underground, highlighting that a critical depth exists for the GFRP anchor. Hence, the ultimate capacity did not change with the anchorage length higher than critical value.

(e) Peak shear stress along depth of GFRP anchors occurred at 0.8 m underground. Therefore, additional reinforcement is required at 0.8 m underground if a GFRP anchor is used in projects.

(f) Force distribution and field photos at failure indicated that shear failure occurred at the GFRP anchor bolt interface at the end of the test.

(g) An elastic mechanical model and Mindlin’s displacement solution are used to get distribution functions of axial force and shear stress along the depth, and the results accord with the test results.

Further studies are required to provide more comprehensive and conclusive observations.

**Data Availability**

The data used to support the findings of this study are included within the article.

**Conflicts of Interest**

The authors declare that they have no conflicts of interest.

**Acknowledgments**

The authors would like to acknowledge the support provided by Natural Science Foundation of China (No. 51078196; No.

41502304) and Natural Science Foundation of Shandong province (No. ZR2016EEQ08) and Science and Technology Project of Shandong province (No. J16LG02).

**References**

- [1] Á. Tóth, Q. Gong, and J. Zhao, “Case studies of TBM tunneling performance in rock-soil interface mixed ground,” *Tunnelling and Underground Space Technology*, vol. 38, pp. 140–150, 2013.
- [2] W. G. Fu, J. G. Liu, and Z. Y. Yang, “Formulae for calculating stability of anti-floating anchor and anchor,” *Chinese Journal of Geotechnical Engineering*, vol. 36, no. 11, pp. 971–1983, 2014.
- [3] J.-N. Ye and G.-B. Liu, “Anti-floating safety design of structures in metro station considering friction resistance enclosure protection,” *Rock and Soil Mechanics*, vol. 31, no. 1, pp. 279–283, 2010.
- [4] X. Zeng, M. Lei, W. J. Zhang, and W. Z. Ji, “Discussion about “time bomb” question for bolt -an Answer to Professor Guo Ying zhong,” *Chinese Journal of Rock Mechanics and Engineering*, vol. 21, no. 01, pp. 143–147, 2002.
- [5] M. Pan and X. Xu, “Experimental study on bond characteristics of adhering sand and ribbed surface FRP bars with concrete,” *Destech Transactions on Engineering and Technology Research*, 2017.
- [6] B. Benmokrane, B. Zhang, A. Chennouf, and R. Masmoudi, “Evaluation of aramid and carbon fibre reinforced polymer composite tendons for prestressed ground anchors,” *Canadian Journal of Civil Engineering*, vol. 27, no. 5, pp. 1031–1045, 2000.
- [7] B. Benmokrane, H. Xu, and E. Bellavance, “Bond strength of cement grouted Glass Fibre Reinforced Plastic (GFRP) anchor bolts,” *International Journal of Rock Mechanics and Mining Sciences & Geomechanics Abstracts*, vol. 33, no. 5, pp. 455–465, 1996.

- [8] H. Ashrafi, M. Bazli, and A. V. Oskouei, "Enhancement of bond characteristics of ribbed-surface GFRP bars with concrete by using carbon fiber mat anchorage," *Construction and Building Materials*, vol. 134, pp. 507–519, 2017.
- [9] M. Bazli, H. Ashrafi, and A. V. Oskouei, "Experiments and probabilistic models of bond strength between GFRP bar and different types of concrete under aggressive environments," *Construction and Building Materials*, vol. 148, pp. 429–443, 2017.
- [10] Y. S. Kim, H. J. Sung, H. W. Kim, and J. M. Kim, "Monitoring of tension force and load transfer of ground anchor by using optical FBG sensors embedded tendon," *Smart Structures and Systems*, vol. 7, no. 4, pp. 303–317, 2011.
- [11] H.-J. Sung, T. M. Dob, J.-M. Kim, and Y.-S. Kim, "Long-Term monitoring of ground anchor tensile forces by FBG sensors embedded tendon," *Smart Structures and Systems*, vol. 19, no. 3, pp. 269–277, 2017.
- [12] M. Y. Zhang, J. Zhang, and J. W. Liu, "Experimental investigation on anti-floating anchor in moderately weathered granite," *Chinese Rock Mechanism and Engineering*, pp. 2741–2746, 2008.
- [13] The Professional Standards Compilation Group of People's Republic of China, *Technical Specification for Retaining and Protection of Building Foundation Excavations*, China Architecture and Building Press, Beijing, China, 2005.
- [14] X. Bai, M. Zhang, and L. Zhu, "Experimental study on shear characteristics of interface of full-bonding glass fiber reinforced polymer anti-floating anchors," *Chinese Journal of Rock Mechanics & Engineering*, 2018.
- [15] E. A. Ahmed, B. Benmokrane, and M. Sansfaçon, "Case study: design, construction, and performance of the la chancelière parking garage's concrete flat slabs reinforced with GFRP bars," *Journal of Composites for Construction*, vol. 21, no. 1, pp. 6001–6013, 2017.
- [16] J. Li, T. Li, and H. Zhu, "Experimental study on enhancement of additional rib to anchorage performance of frp bar," *Journal of Nanjing Tech University*, 2017.
- [17] C. You, "Mechanical analysis on wholly grouted anchor," *Chinese Journal of Rock Mechanics & Engineering*, vol. 21, no. 01, pp. 143–147, 2000.
- [18] E. Kamke, *Ordinary Differential Equation Manual*, China Science Publishing & Media Ltd., 1977.

